2020 SCEC Report

Modeling the 2019 Ridgecrest earthquake sequence with fault geometry that matches both surface rupture and seismicity

PI: David D. Oglesby, Department of Earth and Planetary Sciences, University of California, Riverside

Co-PI: Abhijit Ghosh, Department of Earth and Planetary Sciences, University of California, Riverside

Co-PI: Kyriakopoulos, Center for Earthquake Research and Information, University of Memphis

Amount awarded: $35,000 (UCR)

Proposal Category: B (Integration and Theory)

SCEC Science Priorities:

P1.d. Quantify stress heterogeneity on faults at different spatial scales, correlate the stress concentrations with asperities and geometric complexities, and model their influence on rupture initiation, propagation, and arrest.

P3.a. Refine the geometry of active faults across the full range of seismogenic depths, including structures that link and transfer deformation between faults.

P2.e. Describe how fault geometry and inelastic deformation interact to determine the probability of rupture propagation through structural complexities, and determine how model-based hypotheses about these interactions can be tested by the observations of accumulated slip and paleoseismic chronologies.

P4.a. Determine the relative roles of fault geometry, heterogeneous frictional resistance, crustal material heterogeneities, intrinsic attenuation, shallow crust nonlinearities and ground surface topography in controlling and bounding ground motions,

P1.e. Evaluate how the stress redistribution among fault segments depends on time, at which levels it can be approximated by quasi-static and dynamic elastic mechanisms, and to what degree inelastic processes contribute to stress evolution.

Background

The 2019 Ridgecrest earthquake sequence was a remarkable event in a number of ways. It consisted of two large earthquakes (the largest to hit Southern California in decades) and numerous small-to-moderate sized earthquakes on a complicated criss-cross of nearly-parallel and nearly-perpendicular fault segments, with branches and stepovers at multiple scales. Figure 1 [*Cortez et al.*, 2021] displays the mapped surface fault geometry [*Kendrick et al.*, 2019; *Ponti et al.*, 2020] as well as the aftershock distribution [*SCECDC*, 2013], indicating that the aftershocks do not necessarily line up perfectly with the apparent surface faulting. The first event in this sequence, an M6.4 earthquake, largely took place on a set of left-lateral faults striking to the NE, with a roughly 1.5 km extensional stepover near the NE limit of the quake. The left-lateral fault traces are defined by significant surface faulting evidence, seismological and geodetic models [e.g., *Ross et al.*, 2019; *Li et al.*, 2020; *Pollitz et al.*, 2020; *Wang et al.*, 2020] and aftershock studies [*Lomax*, 2020; *Shelly*, 2020] imply that the M6.4 rupture may have initiated on a buried right-lateral fault segment that intersects the left-lateral fault almost orthogonally in the stepover region, toward the NE edge of the left-lateral fault system. Around 30 hours later, an M 5.4 aftershock took place to the NW of the edge of the possible right-lateral segment of the M6.4 earthquake. Finally, 6 hours after the M5.4 event, an M7.1 earthquake nucleated a short distance to the west of the M5.4, and propagated on a SE-striking right-lateral system of faults that intersected the original M6.4 fault system and continued beyond to the SE for a number of km. It is notable that the M7.1 event did not appear to re-rupture the right-lateral segment that participated in the M6.4 quake, but rather took a more southwest branch to cross the left-lateral fault (as indicated by distinct aftershock clouds from the two events). Due to their close proximity in space and time, these events clearly were linked in some way, but the nature of the coseismic and post-seismic stress interactions between them are still unclear. Investigating the relationship between these large earthquakes by using 3D dynamic rupture modeling is the subject of our funded work.

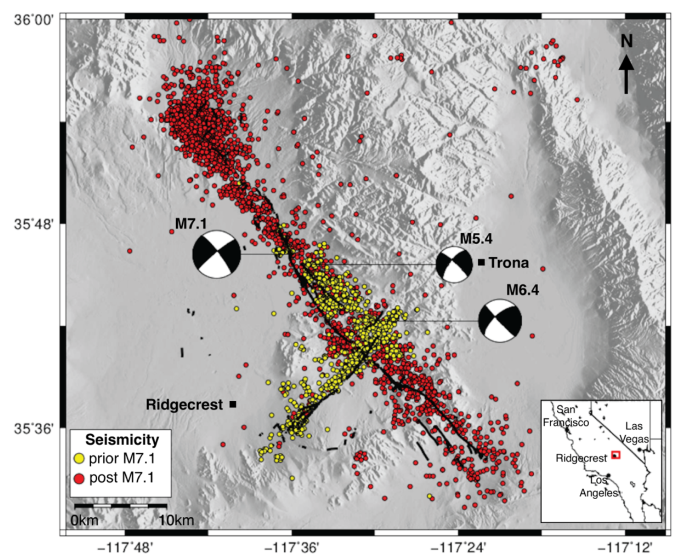

Figure 1. Mapped surface rupture (black curves) [*Kendrick et al.*, 2019; *Ponti et al.*, 2020], main earthquakes displayed by focal mechanisms, and aftershocks [*SCECDC*, 2013] color-coded by timing (yellow: prior to M7.1 earthquake; red: after M7.1 earthquake). Nearby towns shown by name. From [*Cortez et al.*, 2021].

Current Work

With SCEC funding, we completed our initial 3D dynamic finite element [*Barall*, 2009] modeling work on the Searles Valley Earthquake and published it in *Cortez et al.* [2021]. We found that the ability of our models to produce the observed rupture pattern in the M6.4 event and not produce rupture on the M7.1 fault hinged on the pre-stress level of the system, and (perhaps surprisingly) on the depth of burial of the blind nucleating right-lateral fault in the M6.4 event. We found that only a narrow range of initial stress levels would allow rupture to propagate across the M6.4 fault

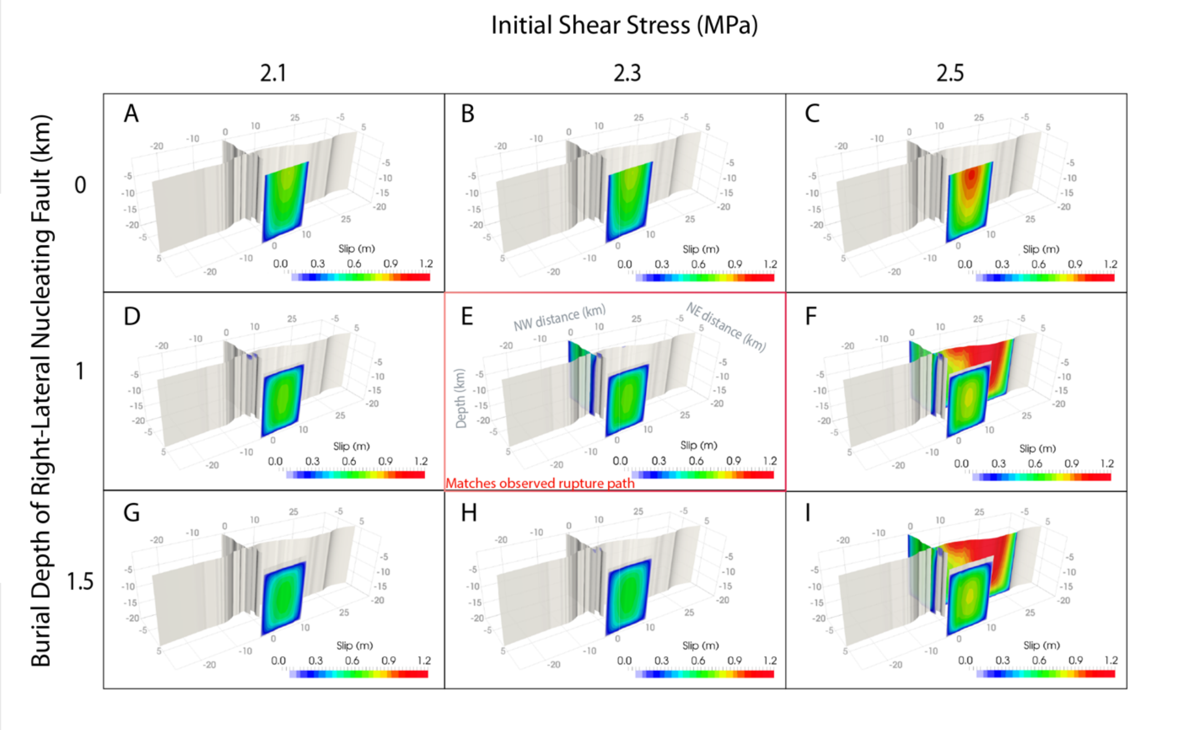

Figure 2. Slip on fault system for three different constant initial shear traction levels (2.1, 2.3, and 2.5 MPa, columns) and three different depths of burial of the right-lateral nucleating segment (0 km, 1 km, and 1.5 km, rows). The model in the center panel (2.3 MPa shear stress, 1 km depth) is the only model that matches the observed rupture propagation pattern for the M6.4 earthquake (indicated by the red boundary box). [*Cortez et al.*, 2021].

system and not the M7.1 system, and also that only a narrow range of burial depths of the nucleating segment would permit this behavior as well. In particular, if rupture is allowed to propagate to the surface of the nucleating fault, rupture is almost always confined to this nucleating segment, avoiding the main M6.4 left-lateral fault structures, in conflict with observations. This faulting behavior is illustrated in Figure 2.

The main goal of the currently supported work is two-fold: to examine how the M6.4 event affected the subsequent rupture and slip pattern of the M7.1 event (through the transfer of stress), and to investigate the effects of more realistic fault geometries on the entire sequence. In the latter case, our plan is to model a fault system that conforms to the mapped surface rupture at shallow depth, but transitions at greater depth to simpler surfaces that more accurately match the aftershock sequences.

Unfortunately, due to campus closures and other COVID-related difficulties, we were unable to make progress on the latter (fault geometry) goal in this past year. However, we were able to make preliminary models of the M7.1 event with and without stress transfer from the earlier M6.4 event. We find that the slip in the M6.4 event significantly alters the shear and normal stress distributions on the M7.1 fault, particularly near their intersection, and on the portion of the M7.1 fault that overlaps with the right-lateral, buried, nucleating segment of the M6.4 fault (Figure 3). In particular, the right-lateral segment of the M6.4 puts the overlapping region on the M7.1 fault in a shear stress shadow, hindering rupture and slip in this area. The final slip pattern (Figure 4) shows this effect. A constant traction model (with parameters equal to our M6.4 work, and with the M7.1 fault being cut by the M6.4) produces a heterogeneous slip distribution, showing the pure effects

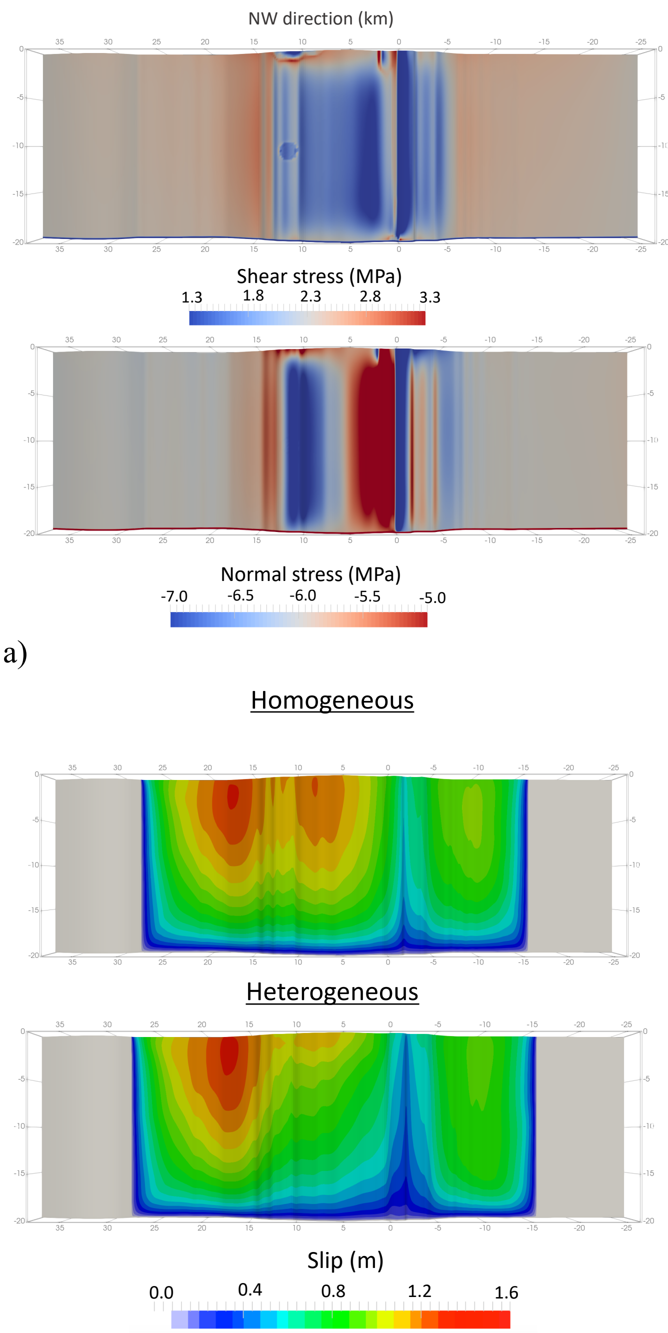

Figure 3. a) Shear and Normal stress increment on M7.1 fault from slip on the preferred M6.4 model. Note the shear stress shadow on the M7.1 in the area in which it overlaps the buried nucleating right-lateral segment of the M6.4 earthquake.
b) Final slip magnitude for homogeneous (top) and heterogeneous (with stress increment from the modeled M6.4 event; bottom) models for the M7.1 Ridgecrest event. Both models display significant slip heterogeneity due to the non-planar M7.1 fault structure; the heterogeneous stress model displays smaller slip where it is shadowed by the M6.4 event.

of the interaction between the fault's slip and its own stress field. There is more slip on the NW portion of the fault, and smaller slip on the SW portion, in agreement with observations. The model that incorporates the final (static) stress transfer from our M6.4 model on top of the initial constant traction assumption produces a somewhat similar final slip patter, but with significantly less slip in the area overlapping the buried right-lateral M6.4 segment.

We plan to implement our improved fault geometry as soon as possible, and complete the work on this project over the following months.

References

Barall, M. (2009), A grid-doubling technique for calculating dynamic three-dimensional spontaneous rupture on an earthquake fault, *Geophysical Journal International*, *178*, 845-859.

Cortez, J. T., D. D. Oglesby, C. Kyriakopoulos, B. Wu, K. Chaudhuri, A. Ghosh, and R. Douilly (2021), On the rupture propagation of the 2019 M6. 4 Searles Valley, California, Earthquake, and the lack of immediate triggering of the M7. 1 Ridgecrest Earthquake, *Geophysical Research Letters*, *48*(4), e2020GL090659.

Kendrick, K. J., S. O. Akciz, S. J. Angster, J.-P. Avouac, J. Bachhuber, S. E. Bennett, et al. (2019), Geologic observations of surface fault rupture associated with the Ridgecrest M6.4 and M7.1 earthquake sequence by the Ridgecrest Rupture Mapping Group, paper presented at 2019 SCEC Annual Meeting, Palm Springs, CA.

Li, S., G. Chen, T. Tao, P. He, K. Ding, R. Zou, et al. (2020), The 2019 Mw 6.4 and Mw 7.1 Ridgecrest earthquake sequence in Eastern California: rupture on a conjugate fault structure revealed by GPS and InSAR measurements, *Geophysical Journal International*, *221*, 1651-1666, doi:10.1093/gji/ggaa099.

Lomax, A. (2020), Absolute location of 2019 Ridgecrest seismicity reveals a shallow Mw 7.1 hypocenter, migrating and pulsing Mw 7.1 foreshocks, and duplex Mw 6.4 ruptures, *Bulletin of the Seismological Society of America*, *XX*, doi:10.1785/0120200006.

Pollitz, F. F., J. R. Murray, J. L. Svarc, C. Wicks, E. Roeloffs, S. E. Minson, et al. (2020), Kinematics of Fault Slip Associated with the 4–6 July 2019 Ridgecrest, California, Earthquake Sequence, *Bulletin of the Seismological Society of America*.

Ponti, D. J., J. L. Blair, C. M. Rosa, K. Thomas, A. J. Pickering, S. Akciz, et al. (2020), Documentation of Surface Fault Rupture and Ground-Deformation Features Produced by the 4 and 5 July 2019 M w 6.4 and M w 7.1 Ridgecrest Earthquake Sequence, *Seismological Society of America*, *91*(5), 2942-2959.

Ross, Z. E., B. Idini, Z. Jia, O. L. Stephenson, M. Zhong, X. Wang, et al. (2019), Hierarchical interlocked orthogonal faulting in the 2019 Ridgecrest earthquake sequence, *Science*, *366*, 346-351.

SCECDC (2013), Southern California Earthquake Data Center, *Caltech.Dataset*, doi:10.7909/C3WD3xH1.

Shelly, D. R. (2020), A high-resolution seismic catalog for the initial 2019 Ridgecrest earthquake sequence: foreshocks, aftershocks, and faulting complexity, *Seismological Research Letters*, *XX*, doi:10.1785/0220190309.

Wang, K., D. S. Dreger, E. Tinti, R. Bürgmann, and T. Taira (2020), Rupture Process of the 2019 Ridgecrest, California Mw 6.4 foreshock and Mw 7.1 earthquake constrained by seismic and geodetic data, *Bulletin of the Seismological Society of America*, *XX*, 1-24, doi:10.1785/0120200108.